



Article

Predictive Voltage Control in Multi-Modular Matrix Converters under Load Variation and Fault Scenario

David Caballero ¹, Sergio Toledo ¹, Edgar Maqueda ¹, Magno Ayala ¹, Raúl Gregor ¹, Marco Rivera ^{2,3,*} and Patrick Wheeler ²

¹ Department of Electronics and Mechatronics Engineering, Facultad de Ingeniería, Universidad Nacional de Asunción, Isla Bogado, Luque 110948, Paraguay; dcaballero@ing.una.py (D.C.); stoledo@ing.una.py (S.T.); emaqueda@ing.una.py (E.M.); mayala@ing.una.py (M.A.); rgregor@ing.una.py (R.G.)

² Power Electronics, Machines and Control (PEMC) Research Group, Faculty of Engineering, Department of Electrical and Electronic Engineering, University of Nottingham, 15 Triumph Rd, Lenton, Nottingham NG7 2GT, UK; pat.wheeler@nottingham.ac.uk

³ Laboratorio de Conversión de Energías y Electrónica de Potencia (LCEEP), Vicerrectoría Académica, Universidad de Talca, 2 Norte # 685, 3460000 Talca, Chile

* Correspondence: marco.rivera@nottingham.ac.uk or marcoriv@utalca.cl

Abstract: This paper presents a model predictive control (MPC) strategy to regulate output voltages in a multi-modular matrix converter topology for isolated loads. The converter system harnesses power from a six-phase permanent magnet synchronous generator (PMSG) to deliver sinusoidal voltages to a three-phase load, with LC filters positioned at the output of each MC module within the multi-modular scheme. The proposed MPC approach ensures that the output voltages remain within acceptable ranges of magnitude, phase, and frequency, even under load variations and system faults. This control strategy is particularly suitable for uninterruptible power supply systems, microgrids or other applications where voltage regulation is critical. Experimental studies validate the effectiveness of the control strategy under various load conditions, reference voltage changes, and simulated system fault scenarios. The results highlight the robustness and reliability of the proposed voltage control using the multi-modular matrix converter.

Keywords: multi-modular matrix converters; predictive voltage control



Citation: Caballero, D.; Toledo, S.; Maqueda, E.; Ayala, M.; Gregor, R.; Rivera, M.; Wheeler, P. Predictive Voltage Control in Multi-Modular Matrix Converters under Load Variation and Fault Scenario.

Technologies **2024**, *1*, 170.

<https://doi.org/10.3390/technologies12090170>

Academic Editor: Dongran Song

Received: 12 July 2024

Revised: 10 September 2024

Accepted: 13 September 2024

Published: 19 September 2024



Copyright: © 2024 by the authors. Licensee MDPI, Basel, Switzerland. This article is an open access article distributed under the terms and conditions of the Creative Commons Attribution (CC BY) license (<https://creativecommons.org/licenses/by/4.0/>).

1. Introduction

The growing demand for reliable and efficient energy systems in isolated environments has driven research into microgrids that harness renewable sources, such as wind energy [1–3]. These microgrids not only provide a clean and sustainable energy source but also enhance the resilience of the electrical system by operating independently during disruptions to the main grid or natural disasters [4–6]. Microgrids are a key focus of research as they provide an integrated platform for managing distributed generation, storage devices, end-user loads, and power converters within a compact space, making them practical alternatives to traditional grids [7–9]. They can operate in either grid-connected or islanded mode, depending on generation capacity, grid integration, and consumer needs. In islanded mode, they must maintain high-quality output voltage, with low harmonic distortion and a fast dynamic response to fluctuations in generation or load dynamics [10,11].

In the context of wind energy generation, multiphase machines are gaining increasing attention due to their significant advantages, including enhanced fault tolerance and reduced current ratings for the same power levels [12–14]. These machines can continue to operate even after one or more open phase faults without the need for additional hardware. Compared to traditional three-phase drives, they also offer reduced torque harmonics, lower power ratings per phase, lower wiring costs, and smaller DC link capacitors [15–17].

Converting the electricity generated in distributed generation systems that make up a microgrid into a form that can be used by the electrical grid or isolated loads is generally

carried out in two stages: a conversion from AC to DC, and then a conversion from DC to AC to match the desired electrical conditions. Different types of power converters have been used for this, including Active Front End (AFE), cascaded multilevel converters, Neutral-Point Clamped (NPC) topologies, and modular multilevel converters [18–21]. However, these converters usually require energy storage, which can add weight, volume, and increase the risk of failure. To solve this problem, researchers are developing a new type of power interface based on a modular architecture that can connect AC sources to loads without using energy storage. The matrix converter (MC) is a promising solution that uses fully controlled bidirectional switches to provide a three-phase sinusoidal voltage with variable amplitude and frequency [22,23]. Different control methods have been proposed, such as PWM, SVM, fuzzy control, and model predictive control (MPC). MPC is a direct control strategy that can reduce complexity and consider multiple control objectives and constraints using different cost functions. It provides fast and accurate performance in both the transient and steady states and has a high controller bandwidth [24,25].

Multi-modular matrix converters (M-MMC) are a novel electric power conversion technology that has numerous advantages, including high efficiency, harmonic reduction, increased reliability and scalability. They have gained significant popularity as an energy conversion technology in applications that require high availability and are sensitive to power quality. For instance, ref. [26] introduces a speed control method for a six-phase induction motor powered by an M-MMC, and ref. [27] presents a current control approach. However, no research has been conducted on the subject of voltage control.

This paper addresses the specific challenge of voltage control in systems powered by a six-phase Permanent Magnet Synchronous Generator (PMSG), which operates independently of the main power grid. The key innovation of this work lies in the integration of the PMSG with two matrix converter (MC) modules within a multi-modular architecture. This novel approach leverages control structures traditionally applied to three-phase systems and extends their benefits to more complex multi-modular configurations, such as the proposed M-MMC. The primary contribution of this research is the development of a high-fidelity voltage control method based on the explicit predictive model of the output filters to achieve voltage levels that exhibit high reliability. The proposed system has been rigorously tested under various scenarios, including fluctuations in generation and load, as well as potential failures in the MC modules. Furthermore, this paper presents a comprehensive analysis of the robustness of the proposed control scheme in the face of these challenges, along with a detailed study of the system's complexity. The results underscore the system's ability to maintain stable performance under adverse conditions, making it a promising solution for isolated power systems.

The structure of the remainder of the paper is as follows: Section 2 describes the conversion scheme and the proposed control strategy; the design of the experimental bench and the main results are presented in Section 3. In Section 4, the obtained results are discussed, and an analysis of the complexity of the proposed system is carried out. Finally, Section 5 offers a summary and the main conclusions of the work.

2. Proposed Predictive Voltage Control

This article proposes a predictive voltage control (PVC) scheme for an M-MMC with LC output filter. The MPC technique utilizes a mathematical model of the system to predict how the controlled variables will behave in the future. The discrete nature of power converters simplifies the MPC optimization algorithm by allowing it to predict the system's behavior for only a limited set of possible switching states. This approach is known as finite control set MPC (FCS-MPC). In this particular case, for PVC, the following steps are taken to apply FCS-MPC: (i) the matrix converter (MC) is modeled as a finite state system; (ii) the output filter's discrete-time model is used to predict the controlled variable for each possible switching state; (iii) the desired system response is defined by a cost function; and (iv) the switching state that minimizes the cost function is selected for the next sampling period. The following subsections will provide more detailed explanations of each of these steps.

2.1. Finite-State Model of the MC

To apply PVC, the MC is first modeled as a finite state system, which means that it is represented as a set of discrete states that it can occupy. This model should include the dynamics of the converter, the switching states, and any relevant constraints. In the proposed topology, a passive input filter is employed to connect two three-phase MC modules to a single three-phase source. This topology can be seen in Figure 1. On the other hand, an output filter (LC) is utilized to link the MC modules to the load. The AC source produces voltages denoted $u_x, v_x,$ and w_x , where $x \in 1,2$ indicates the respective module. The MC input voltages are v_{ixu}, v_{ixv} and v_{ixw} , and the input currents are also $i_{ixu}, i_{ixv},$ and i_{ixw} , respectively. The MC output voltages with respect to the corresponding neutral point (N_1 or N_2) are v_{oxa}, v_{oxb} and v_{oxc} . Moreover, the MC output currents are i_{Lxa}, i_{Lxb} and i_{Lxc} , respectively.

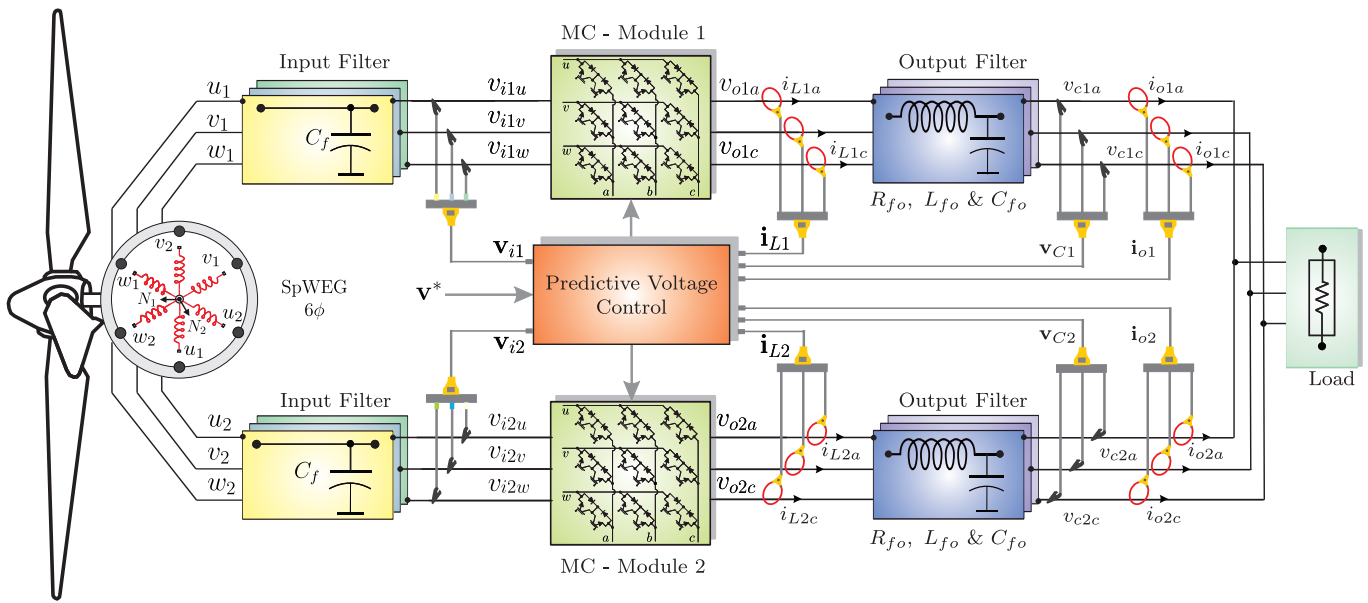


Figure 1. Proposed PVC overall scheme.

If the voltage and current vector sets for the three phases are defined as:

$$\mathbf{v}_{ix} = \begin{bmatrix} v_{ixu} \\ v_{ixv} \\ v_{ixw} \end{bmatrix}, \quad \mathbf{v}_{ox} = \begin{bmatrix} v_{oxa} \\ v_{oxb} \\ v_{oxc} \end{bmatrix},$$

$$\mathbf{i}_{ix} = \begin{bmatrix} i_{ixu} \\ i_{ixv} \\ i_{ixw} \end{bmatrix}, \quad \mathbf{i}_{Lx} = \begin{bmatrix} i_{Lxa} \\ i_{Lxb} \\ i_{Lxc} \end{bmatrix}, \quad (1)$$

the next set of vector equations establishes a relationship between the input and output voltages and currents of the MC through the switching states:

$$\mathbf{v}_{ox} = \mathbf{S} \cdot \mathbf{v}_{ix}, \quad \mathbf{i}_{ix} = \mathbf{S}^T \cdot \mathbf{i}_{Lx}, \quad (2)$$

where \mathbf{S} represents the instantaneous transfer matrix, which is a mathematical construct that defines the relationship between the input and output variables of an MC at a given instant in time, and is defined as follows:

$$\mathbf{S} = \begin{bmatrix} S_{ua} & S_{ub} & S_{uc} \\ S_{va} & S_{vb} & S_{vc} \\ S_{wa} & S_{wb} & S_{wc} \end{bmatrix}, \quad (3)$$

where $S_{xy} \in \{0, 1\}$ represents the state of the corresponding switch. The switching signals S_{xy} must meet the following requirement in order to prevent short circuits on the input side and guarantee uninterrupted current flow on the load side:

$$S_{uy} + S_{vy} + S_{wy} = 1. \quad y \in \{a, b, c\}. \quad (4)$$

Each MC involves the use of nine controlled bidirectional switches (three for each phase) that are activated in different configurations to facilitate energy conversion. Due to the specific operational constraints imposed on the system, there are only twenty-seven permissible switching states [28].

2.2. Discrete-Time Model of the LC Output Filter

Once the relationships between the input and output variables of the MC modules are established, it is possible to model the output filter. The output filter voltages (i.e., the connected to the load side) are v_{Cxa} , v_{Cxb} and v_{Cxc} , and the output currents of the output filter are given by i_{oxa} , i_{oxb} and i_{oxc} . Expressing the above using vectors in their three phases,

$$\mathbf{v}_{Cx} = \begin{bmatrix} v_{Cxa} \\ v_{Cxb} \\ v_{Cxc} \end{bmatrix}, \quad \mathbf{i}_{ox} = \begin{bmatrix} i_{oxa} \\ i_{oxb} \\ i_{oxc} \end{bmatrix}. \quad (5)$$

Applying Kirchhoff's laws and using Equations (1) and (5), the continuous-time dynamic model of the (LC) passive output filters, shown in Figure 2, is described by vector equations as follows:

$$\mathbf{v}_{ox} - \mathbf{v}_{Cx} = L_{fo} \frac{d\mathbf{i}_{Lx}}{dt} + R_{fo} \mathbf{i}_{Lx}, \quad (6)$$

$$C_{fo} \frac{d\mathbf{v}_{Cx}}{dt} = \mathbf{i}_{Lx} - \mathbf{i}_{ox}, \quad (7)$$

where C_{fo} is the filter's capacitor, and L_{fo} and R_{fo} are the output filter's inductance and leakage resistance, respectively. Next, the continuous-time model should be discretized into a discrete-time model, which is suitable for use in PVC. This involves selecting a sampling time and using numerical methods to approximate the continuous-time dynamics. In this case, the model of the system is derived from the finite-state model of the MC, expressed in Equation (2), the continuous-time model of the output filter, indicated in Equations (6) and (7), and the $(\alpha - \beta)$ transform defined in [29–32] as:

$$\begin{aligned} z_{\alpha} &= \frac{2}{3} \left(z_a - \frac{1}{2} z_b - \frac{1}{2} z_c \right), \\ z_{\beta} &= \frac{2}{3} \left(\frac{\sqrt{3}}{2} z_b - \frac{\sqrt{3}}{2} z_c \right). \end{aligned} \quad (8)$$

$z_{\alpha\beta}$ denotes the voltage or current in the stationary reference frame after the transformation of the respective triphasic variables z_{abc} . Given that all of the parameters are constant throughout all legs, the i_L variable dynamic at the $(\alpha - \beta)$ reference frame is given by:

$$L_{fo} \frac{di_{L\alpha\beta}}{dt} = v_{o\alpha\beta} - v_{C\alpha\beta} - R_{fo} i_{L\alpha\beta}. \quad (9)$$

On the other hand, the dynamic behaviour of the voltage through the capacitor v_C of the filter is defined as follows:

$$C_{fo} \frac{dv_{C\alpha\beta}}{dt} = i_{L\alpha\beta} - i_{o\alpha\beta}. \quad (10)$$

In this way, the system's state-space representation, obtained from Equations (9) and (10), is given by:

$$\dot{\mathbf{x}} = \mathbf{Ax} + \mathbf{Bu}, \quad (11)$$

where:

$$\dot{\mathbf{x}} = \begin{bmatrix} \dot{i}_{L\alpha\beta} \\ \dot{v}_{C\alpha\beta} \end{bmatrix}, \quad \mathbf{x} = \begin{bmatrix} i_{L\alpha\beta} \\ v_{C\alpha\beta} \end{bmatrix}, \quad \mathbf{u} = \begin{bmatrix} v_{o\alpha\beta} \\ i_{o\alpha\beta} \end{bmatrix},$$

$$\mathbf{A} = \begin{bmatrix} -\frac{R_{fo}}{L_{fo}} & -\frac{1}{L_{fo}} \\ \frac{1}{C_{fo}} & 0 \end{bmatrix}, \quad \text{and} \quad \mathbf{B} = \begin{bmatrix} \frac{1}{L_{fo}} & 0 \\ 0 & -\frac{1}{C_{fo}} \end{bmatrix}. \quad (12)$$

The equations mentioned describe the continuous time model for the output filters of each MC module. This model takes into account the voltage across each capacitor $v_{C\alpha\beta}$ and the output current $i_{L\alpha\beta}$ as state variables. Finally, the discrete model of the system is given by

$$\mathbf{x}(k+1) = \mathbf{A}_q \mathbf{x}(k) + \mathbf{B}_q \mathbf{u}(k), \quad (13)$$

being

$$\mathbf{A}_q = e^{\mathbf{A}T_s}, \quad \text{and} \quad \mathbf{B}_q = \int_0^{T_s} e^{\mathbf{A}(T_s-\tau)} \mathbf{B} d\tau.$$

\mathbf{A} and \mathbf{B} are given by Equation (12) and T_s is the sampling time, and the selected value for it will be discussed in the following section.

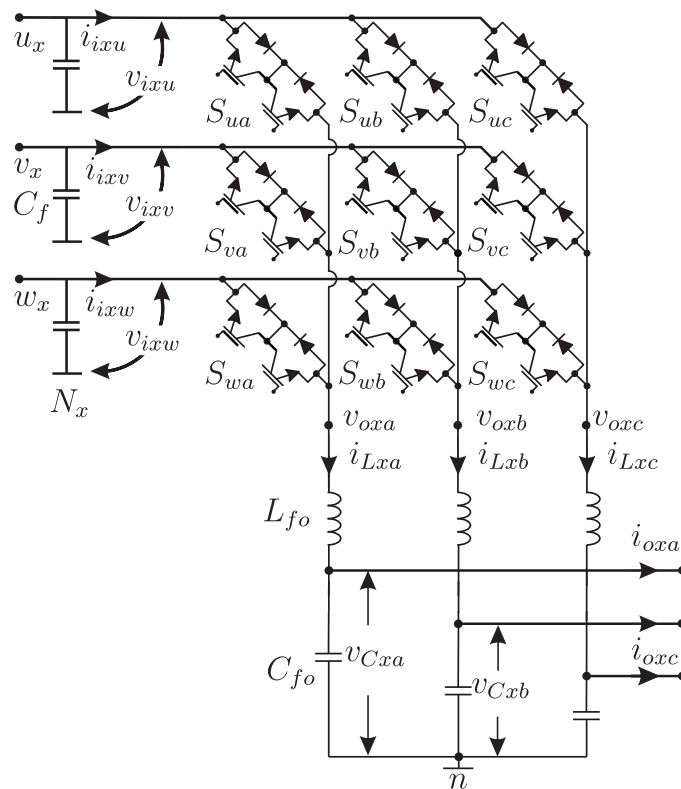


Figure 2. Topology of the MC module with LC filter.

2.3. Prediction Model

The prediction model in this PVC strategy is used to predict how process variables will change in the future. Thus, by using the discrete model that describes the system dynamics, it is possible to predict the states of i_L and v_C as follows:

$$i_{L\alpha\beta}(k+1) = a_{11}i_{L\alpha\beta}(k) + a_{12}v_{C\alpha\beta}(k) + b_{11}v_{o\alpha\beta}(k) + b_{12}i_{C\alpha\beta}(k) \quad (14)$$

$$v_{C\alpha\beta}(k+1) = a_{21}i_{L\alpha\beta}(k) + a_{22}v_{C\alpha\beta}(k) + b_{21}v_{o\alpha\beta}(k) + b_{22}i_{C\alpha\beta}(k) \quad (15)$$

being

$$\mathbf{A}_q = \begin{bmatrix} a_{11} & a_{12} \\ a_{21} & a_{22} \end{bmatrix}, \mathbf{B}_q = \begin{bmatrix} b_{11} & b_{12} \\ b_{21} & b_{22} \end{bmatrix},$$

where k indicates the present sample period and $k + 1$ denotes the start of the next sampling time. As from the preceding equations it is possible to predict the values of the current at the inductor and the output voltage in order to use them in the implementation of the predictive control. The prediction model used, is a discrete-time model that considers the effects of the system dynamics and external disturbances.

2.4. Cost Function

The main objective of the PVC is to quickly and accurately track the reference voltage \mathbf{v}^* in response to changes in amplitude, frequency, and phase shift, as well as to changes in the conditions of the load connected to the system. To achieve this objective, PVC uses a finite set of voltage vectors that can be applied to each MC module. The control algorithm optimizes the selection of these vectors over a future prediction horizon to minimize a cost function that represents the tracking error. In this case, each module is considered independently, keeping the voltage at the output of each filter constant and injecting half of the total current required by the load. This control is carried out using the following cost function:

$$\begin{aligned} g_1 &= (v_\alpha^* - v_{c1\alpha})^2 + (v_\beta^* - v_{c1\beta})^2, \\ g_2 &= (v_\alpha^* - v_{c2\alpha})^2 + (v_\beta^* - v_{c2\beta})^2, \end{aligned} \quad (16)$$

where v_α^* , and v_β^* represent the reference voltages in the $\alpha - \beta$ coordinate system, while $v_{c1\alpha}$, $v_{c2\alpha}$, $v_{c1\beta}$, and $v_{c2\beta}$ represent the predicted voltages in the $\alpha - \beta$ stationary reference frame.

2.5. Control Process and Switching State Selection Procedure

The control algorithm adjusts the voltage vector selection to keep the filter output voltage for each MC module as close as possible to the reference voltage. A detailed explanation of the switching state selection and control process is shown step by step below:

1. Start: The process begins at the Start block, marking the starting point of the control process and switching state selection procedure.
2. Measurement: At the beginning of each sampling instant (k), the algorithm measures various parameters such as input voltage $v_{ix}(k)$, output filter currents $i_{Lx}(k)$ and $i_{ox}(k)$, and output voltage $v_{Cx}(k)$ for each phase a, b, c . These measurements are then transformed into the $(\alpha - \beta)$ subspace to simplify calculations. After transformation, the values are discretized for processing.
3. Prediction calculation: With the measured and discretized values, the predicted currents i_{Lx}^{k+1} and voltages v_{Cx}^{k+1} are calculated using Equations (14) and (15), respectively, and the reference values v_{ox}^{opt} .
4. Variable initialization: The variables g_1^{opt} and g_2^{opt} are initialized to infinity (∞). This is a preparatory step for later optimization.
5. Initial iteration: Set $j = 0$, indicating the start of an iteration cycle that will be key for optimization.
6. Increment j : The counter j is incremented in each iteration, moving to the next set of values to be evaluated.
7. Output vector calculation: The voltage vector v_{ox} is calculated using the value S_j from the current iteration.
8. Future current and voltage calculation: With v_{ox} calculated, the predicted values of the current i_{Lx}^{k+2} and the voltage v_{Cx}^{k+2} for the next step are determined.
9. Objective functions calculation: The objective functions g_1 and g_2 are calculated, which will be used to determine how optimal the calculated voltage vector is.
10. Evaluation and update of g_1^{opt} : If g_1 is less than g_1^{opt} , then update g_1^{opt} and save S_j as S_1^{opt} , along with the voltage v_{o1}^{opt} .

11. Evaluation and update of g_2^{opt} : Similarly, if g_2 is less than g_2^{opt} , then update g_2^{opt} , S_j as S_2^{opt} , and v_{o2}^{opt} .
12. Iteration limit check: Check if the counter j has reached the value 27, which would indicate that all possible combinations have been evaluated.
13. Application of optimal vector: If the limit has been reached, apply the optimal vector S^{opt} , which is selected from S_1^{opt} and S_2^{opt} , depending on which better minimizes the objective functions.
14. Wait for next cycle: The process stops and waits until the next sampling time, at which point the entire cycle will be repeated for a new prediction and optimization.

The described process is iterative; key system variables are measured, predictions are made for future voltage and current values, and the best control option is selected through an optimization process. The flow diagram corresponding to the described control strategy is presented in Figure 3.

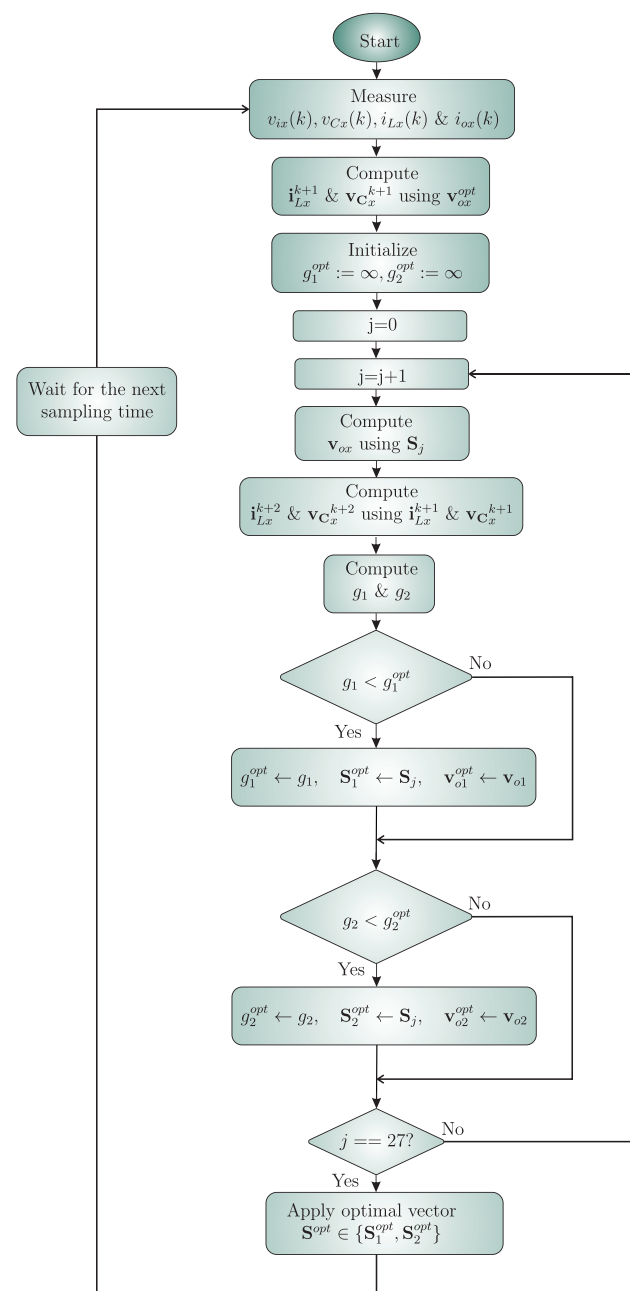


Figure 3. PVC process and switching state selection flowchart.

3. Results

Experimental tests were conducted to evaluate the proposed topology in this paper, using the setup depicted in Figure 1. The experimental setup consists mainly of two MC modules, each with three phases, which are powered by a six-phase permanent magnet synchronous generator (PMSG). At the output of each MC module, there is an output LC filter, and they are both connected to a single three-phase R-type isolated load. For the control unit, a MicrolabBox device was used in conjunction with a SPARTAN 6 FPGA device, which implements a safe switching strategy for the bidirectional MC switches. Six voltage sensors were used to measure v_{ix} and v_{Cx} , and six current sensors were used to measure i_{L1a} and i_{L2a} . The parameters used for the experimental tests are shown in Table 1. The evaluation of the proposed system in this work was conducted using the experimental setup shown in Figure 4. The system consists of two three-phase matrix converter (MC) modules, each equipped with SiC-MOSFET power semiconductor devices. Each MC module operates independently with its own input and output filters. For the experimental tests of the M-MMC, a six-phase permanent magnet synchronous generator (PMSG) was used as the input source, and a 20 kW three-phase AC variable load bank was employed as the isolated output load. A detailed description of the elements and equipment used in the experimental setup, including their manufacturers, models, types, and specifications, is provided in the Table 2.

Table 1. Electrical parameters.

Parameter	Symbol	Value	Unity
Input frequency	f_s	50	Hz
Input voltage peak	v_s	150	V
Input filter capacitor	C_f	30	μF
Output filter inductor	L_{fo}	10	mH
Output filter capacitor	C_{fo}	20	μF
Load resistance	R	8–16	Ω
Sampling time	T_s	50	μs

Table 2. Description of elements and equipment of the experimental setup.

Element	General Features	Specifications
Matrix Converter	Manufacturer: Rohm Semiconductor. Kyoto, Japan Type: SiC-MOSFET. Model: SCH2080KE [33] Manufacturer: TI. Dallas, Texas, U.S Type: Isolate gate driver. Model: ISO5500 [34]	$V_{DSS} = 1200$ [V], $I_D = 40$ [A] $P_D = 262$ [W] $I_o = 2.5$ [A], $f_{in} = 520$ [kHz] $P_D = 592$ [mW]
Generator	Manufacturer: Qingdao Minshen Wind Power Technology Co., Ltd., Qingdao, China Type: Permanent Magnet Synchronous [35] Generator—(PMSG) Waveform: Trapezoidal	20 [Hp]—Power. 750 [Vrms]—Voltage 50 [Hz]—Frequency 12—Pairs of Poles 8.7180 [Vs]—Magnetic Flux (per phase) 2.205 [Ohm]—Stator Resistance 0.0780 [H]—Stator Inductance
Output Filter	Manufacturer: SIPCON SRL. Luque, Paraguay Inductor. Type: Iron Core Capacitor. Type: Non-polarized	10 [kW], 15 [A], 50 [Hz] 400 [VAC], 50/60 [Hz]
AC Variable Load Bank	Manufacturer: TE Connectivity. Schaffhausen, Switzerland Type: Tubular Ceramic Core Resistor	20 [kW]—Max power 380 [V], 3 Phase, 4 Wires
Control Unit	Manufacturer: dSPACE. Paderborn, Germany Type: MicroLabBox. Model: 1202 [36]	Compatible with Matlab Simulink 2018b 2 GHz dual-core real-time processor 100 I/O channels, Ethernet interfaces

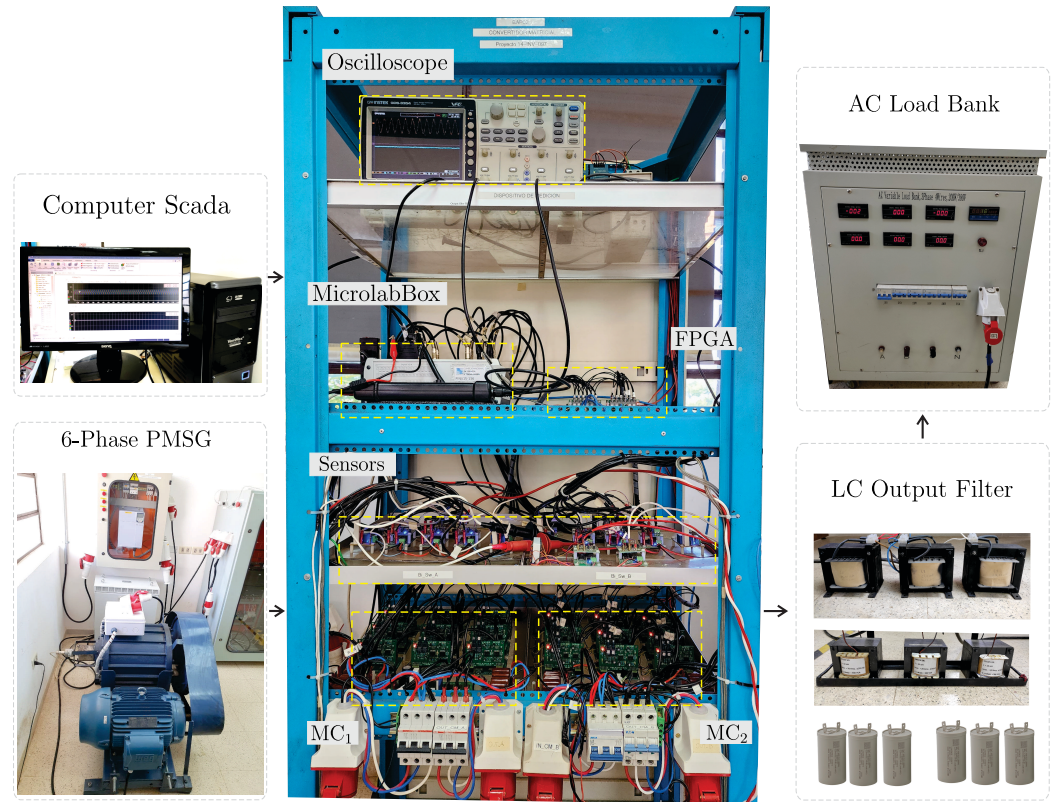


Figure 4. Experimental setup.

In Figure 5, the results of the M-MMC operation using the PVC strategy are presented. Figure 5a,b show the output voltage waveform behavior of each module for a voltage reference equal to 40 V/60 Hz and 100 V/30 Hz, respectively. In both cases, the waveform of the output current i_{ga} feeding the resistive load at the output can be observed in a single phase, similar results were obtained in the other phases. Figure 5c,d correspond to the transient responses of the proposed system for a reference voltage $v^* = 40$ V. Figure 5c represents the response to a change in the reference frequency $f^* = 30$ Hz to $f^* = 60$ Hz and phase shift of 70 degrees, and Figure 5d represents the voltage tracking response at the output versus a change in the amplitude and phase of the reference corresponding to $v^* = 40$ V to $v^* = 50$ V, and a phase shift of 70 degrees. The obtained waveforms show the effort of the implemented predictive control against transient variations in frequency and amplitude of the output voltage.

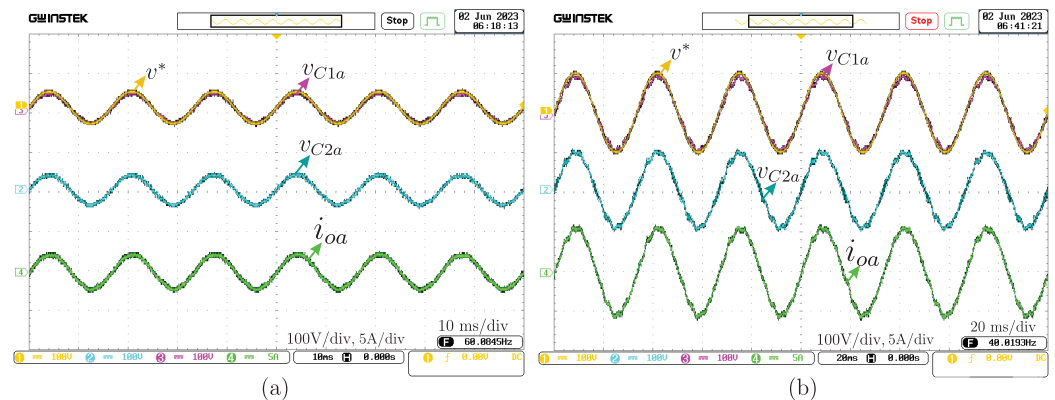


Figure 5. Cont.

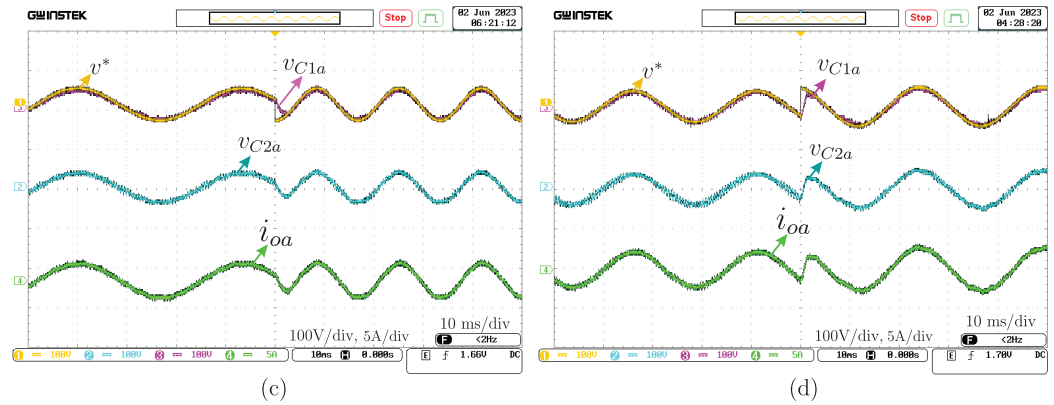


Figure 5. Experimental results of the M-MMC with PVC applied to an isolated load. (a) Steady-state response for $v^* = 40$ V and $f^* = 60$ Hz in both modules. (b) Steady-state response for $v^* = 100$ V and $f^* = 30$ Hz in both modules. (c) Transient response for a change in the reference frequency from $f^* = 30$ Hz to $f^* = 60$ Hz with $v^* = 40$ V and a phase shift of 70 degrees, and (d) Transient response for a change in the reference amplitude from $v^* = 40$ V to $v^* = 50$ V with $f^* = 30$ Hz and a phase shift of 70 degrees.

Tests were conducted on the system to assess its performance under different operating conditions. Specifically, the system was evaluated by varying the output resistive load. Figure 6 the evaluations are observed made to the topology against variations in the output load corresponding to values from $R = 16 \Omega$ to $R = 8 \Omega$. In both figures, the voltage tracking at the output of each module is observed, with a constant behavior in the reference tracking even after the change in the load (increase of the current i_{oa}), for a reference of $v^* = 50$ V and $f^* = 20$ Hz.

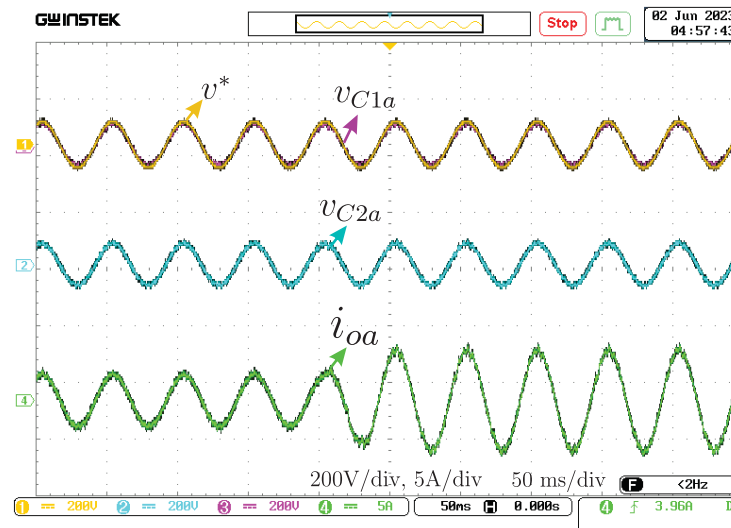


Figure 6. Experimental results of the M-MMC with PVC applied to an isolated load. Response for a step change in the load from $R = 16 \Omega$ to $R = 8 \Omega$, with $f^* = 20$ Hz and $v^* = 50$ V.

Finally, the proposed control strategy for the M-MMC topology was tested under fault conditions. One of the M-MMC modules was deliberately failed during the experiment and the behavior of the control strategy was evaluated. Figure 7 shows the output voltage waveforms of both modules following a 40 V/60 Hz reference. Figure 7a sudden failure of module 2 is observed, with a gradual decrease in voltage v_{C2a} to 0 V. However, the reference voltage tracking of module 1 remains constant before and after the fault event, and Figure 7b module 1 is initially observed with an output voltage equal to 0 V, and at a given moment it is put into operation in order to observe the coupling to module 2, which is in operational from the start of the experiment. In both cases, it is observed that

the waveforms of the output current i_{oa} remains stable, with no significant variations, despite the fault event in one of the modules. These results demonstrate the effectiveness of the proposed control strategy in maintaining system stability and reliability even under fault conditions.

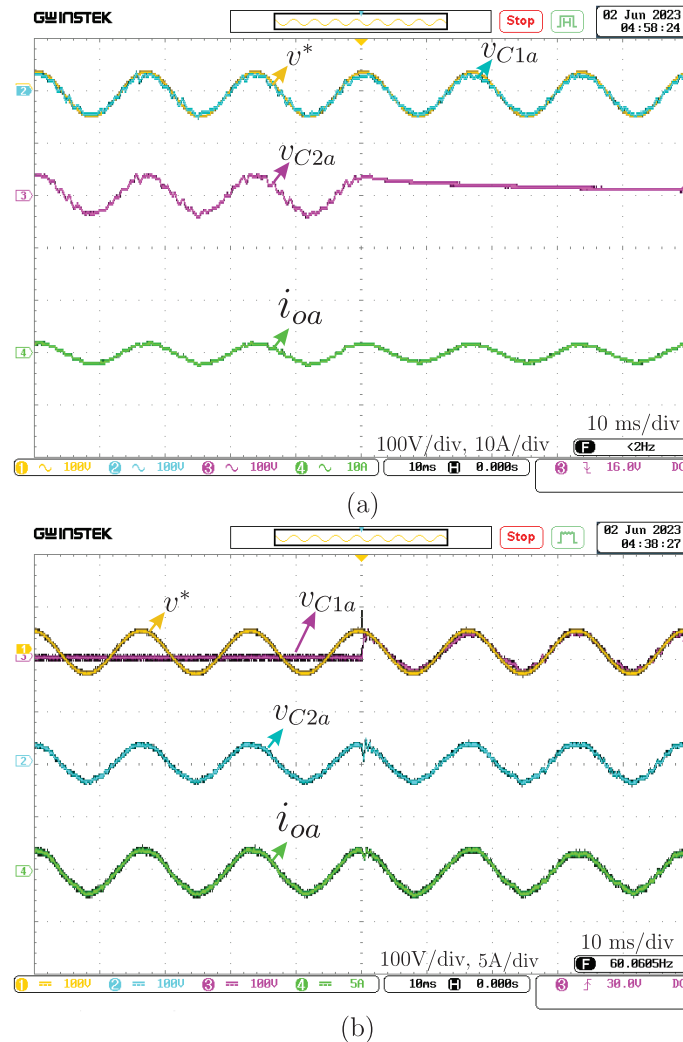


Figure 7. Experimental results of the M-MMC with PVC under fault conditions. (a) Response of the PVC under failure in module 1 of the M-MMC. (b) Response of the PVC at the moment of coupling module 1 with module 2 of the M-MMC.

4. Discussion

The presented results highlight the effectiveness and robustness of the PVC strategy when applied to the M-MMC topology under various operating conditions, including resistive load variations and fault scenarios. The following sections discuss these results and include a study related to the complexity of the proposed topology, associated costs, and failure probability.

4.1. Output Voltage Waveform Behavior

Figure 5a,b illustrate the output voltage waveforms for two different voltage references, 40 V/60 Hz and 100 V/30 Hz, respectively. The observed waveforms demonstrate the M-MMC's ability to maintain constant output voltage waveforms across different modules. This stability is critical for applications requiring precise voltage control and high reliability.

4.2. Transient Response Analysis

The transient responses, as depicted in Figure 5c,d, provide insight into the system's performance during rapid changes in operating conditions. Figure 5c shows the system's response to a frequency change from 30 Hz to 60 Hz and a phase shift of 70 degrees, while Figure 5d demonstrates the voltage tracking response to an amplitude change from 40 V to 50 V and a similar phase shift. The results indicate that the implemented predictive control can effectively manage transient variations, maintaining voltage stability and ensuring accurate tracking of the reference signal.

4.3. Load Variation Performance

The system's response to load variations is examined in Figure 6. The tests involved changing the resistive load from $R = 16 \Omega$ to $R = 8 \Omega$, with a reference voltage of 50 V and a frequency of 20 Hz. Despite the increase in current i_{oa} , the output voltage tracking at each module remained consistent, demonstrating the system's capability to adapt to load changes while maintaining accurate reference tracking. This adaptability is crucial for applications with fluctuating load demands.

4.4. Fault Tolerance

The fault tolerance of the proposed control strategy is evaluated in Figure 7, where one M-MMC module was deliberately disabled. Figure 7a illustrates the sudden failure of module 2, with its voltage v_{C2a} dropping to 0 V. Despite this failure, module 1 continued to accurately track the reference voltage. Figure 7b presents the scenario where module 1, initially at 0 V, was activated to observe its interaction with the operational module 2. In both fault scenarios, the output current i_{oa} remained stable, demonstrating that the control strategy effectively maintained system stability and reliability despite the failure of one module.

The results demonstrate the efficacy of the PVC strategy in ensuring stable operation of the M-MMC topology under various conditions, including different voltage references, transient variations, load changes, and fault scenarios. The ability to maintain accurate voltage tracking and stable current waveforms across these conditions underscores the robustness of the proposed control strategy. These findings are significant for the development of reliable and fault-tolerant power conversion systems in applications where stability and precision are paramount.

4.5. Complexity and Cost of the M-MMC Topology

Finally, it is crucial to discuss the fundamental role of the Permanent Magnet Synchronous Generator (PMSG) in the generation stage, as well as the proposed topology for the conversion stage, based on the Multi-Modular Matrix Converter (M-MMC). Distributing power across a greater number of phases offers significant advantages for medium to high-power applications since the power per phase is reduced for a constant nominal power, allowing for more efficient sizing of power electronics and consequently reducing the associated costs.

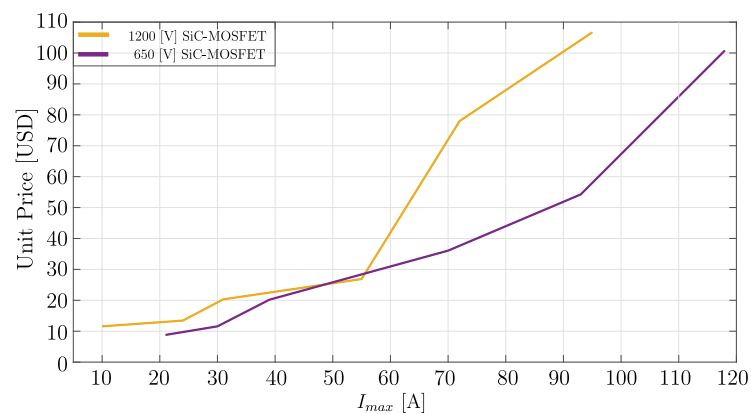
In this context, an analysis of power semiconductor costs based on advanced technologies, such as fourth-generation SiC MOSFETs, was conducted. This study evaluated the semiconductors used in the MC modules that make up the proposed multi-modular topology, considering devices from Rohm and distributed by DigiKey, with the aim of comparing the economic advantages of converting a three-phase system to a six-phase system. Table 3 shows the price list of fourth-generation semiconductors based on SiC-MOSFET technology.

Table 3. Unit price of 4th-Gen SiC-MOSFET semiconductor devices for different maximum currents.

Model	Voltage [V]	Current [A]	Price [USD]
SCT2450KEHRC11	1200	10	11.57
SCT3105KLHRC11	1200	24	13.43
SCT3080KLGC11	1200	31	20.3
SCT3040KLGC11	1200	55	26.87
SCT3030KLGC11	1200	72	77.99
SCT3022KLHRC11	1200	95	106.67
SCT3120ALGC11	650	21	8.8
SCT3080ALGC11	650	30	11.57
SCT3060ALHRC11	650	39	20.18
SCT3030ALHRC11	650	70	36.06
SCT3022ALHRC11	650	93	54.24
SCT3017ALHRC11	650	118	100.8

The study found that the cost of a 55 A device, such as the SCT3040KLGC11, is 26.87 USD, while a 95 A device, like the SCT3022KLHRC11, costs 106.67 USD, both with a maximum operating voltage of 1200 V. For a three-phase system requiring 95 A per phase, and considering that each MC module consists of 18 semiconductors (nine logic switches each composed of two semiconductors), the total semiconductor cost would be 1920.06 USD. However, by converting the system to an equivalent six-phase configuration, 36 devices of 55 A would be needed to handle the same current (allowing up to 110 A in total, which is greater than the 95 A required per phase in the original system). The total cost in this case would be 967.32 USD, resulting in a significant reduction in power semiconductor costs of 952.74 USD. This clearly demonstrates an economic advantage of multi-modular matrix systems compared to traditional matrix converters.

Figure 8 shows the price curve for fourth-generation SiC MOSFET semiconductors as a function of the maximum current they can handle, for two maximum working voltages. This graph, based on data from Rohm and DigiKey prices in August 2024, reveals that for high currents, the price curve becomes exponential, highlighting the importance of current reduction in terms of cost savings.

**Figure 8.** Unit price of SiC-MOSFET 4th Gen semiconductor devices as a function of maximum supported current.

Additionally, the reduction in current per phase allows for higher switching frequencies, which decreases the size of magnetic components and filtering requirements, further increasing the power density of the conversion system [37–39]. Since the cost-to-power handling capacity ratio is not linear, in some applications, reducing the current by half can lead to a significant decrease in implementation costs. Traditionally, power converters have been designed for specific applications, minimizing the number of power devices to reduce the probability of failure and, consequently, operation and maintenance costs. However, this approach limits fault tolerance and converter availability since a component failure

can halt the entire system. Although the proposed topology, based on the M-MMC, incorporates twice as many semiconductors as the MC topology for three-phase systems, which could increase complexity and the probability of failure, it offers significant advantages in terms of availability and costs, as demonstrated in this study. At the analyzed power level, the system presents an even better cost-benefit ratio.

5. Conclusions

This work proposes the implementation of a PVC strategy applied to a multi-modular matrix converter, which serves as a conversion stage to supply sinusoidal voltages to a three-phase load through an output LC filter. The control strategy has been shown to be viable under both transient and steady-state operating conditions. The results demonstrate adequate voltage tracking in response to a reference voltage variation in amplitude, frequency and phase, under different load conditions. Furthermore, the proposed control scheme is robust against fault conditions that may occur in any of the three-phase MC modules, as it can compensate for the power delivered to the load by optimally distributing the current injected into the load through the remaining operational module. The experimental results of the proposed predictive voltage control technique using a multi-modular matrix converter have proven to be viable in applications where high reliability and an adequate voltage harmonic profile are required, such as the integration of renewable energies in microgrids.

Author Contributions: Conceptualization, D.C.; methodology, D.C., S.T., M.R. and P.W.; software, D.C., S.T. and E.M.; validation, E.M. and D.C.; formal analysis, D.C., E.M., S.T. and M.A.; investigation, D.C., S.T. and E.M.; resources, R.G., M.R. and P.W.; data curation, D.C. and E.M.; writing—original draft preparation, D.C., E.M., S.T., M.A. and R.G.; writing—review and editing, M.R., R.G., P.W., S.T. and M.A.; visualization, D.C. and S.T.; supervision, S.T., P.W. and M.R.; project administration, S.T., E.M. and M.R.; funding acquisition, R.G., E.M., M.R. and P.W. All authors have read and agreed to the published version of the manuscript.

Funding: This research received funding from various sources, including the “Programa de Doctorado en Ingeniería Electrónica con Énfasis en Electrónica de Potencia de la Facultad de Ingeniería de la Universidad Nacional de Asunción, POSG16-5, BENA07-4”, the “Programa Paraguayo para el Desarrollo de la Ciencia y Tecnología (PROCIENCIA)”, and the Research Project PINV01-743 of the “Consejo Nacional de Ciencia y Tecnología (CONACYT)”. The authors express their gratitude for the financial support provided by the Agencia Nacional de Investigación y Desarrollo (ANID) FONDECYT Regular grant number 1220556, ANID FOVI230169, Fondap SERC 1523A0006, ENNOBLE-R02401, and the IRCF 24932270 project from the University of Nottingham.

Institutional Review Board Statement: Not applicable.

Informed Consent Statement: Not applicable.

Data Availability Statement: The original contributions presented in the study are included in the article, further inquiries can be directed to the corresponding author/s.

Conflicts of Interest: The authors declare no conflict of interest. The funders had no role in the design of the study; in the collection, analyses, or interpretation of data; in the writing of the manuscript; or in the decision to publish the results.

Abbreviations

The following abbreviations are used in this manuscript:

AFE	Active front end
FCS-MPC	Finite control set model predictive control
M-MMC	Multi-modular matrix converter
MOSFET	Metal-oxide-semiconductor field-effect transistor
NPC	Neutral point clamped
PVC	Predictive voltage control

PWM	Pulse with modulation
SiC	Silicon carbide
SVM	Space vector modulation

References

- Abdelsattar, M.; Ismeil, M.A.; Aly, M.M.; Abu-Elwfa, S.S. Energy Management of Microgrid with Renewable Energy Sources: A Case Study in Hurghada Egypt. *IEEE Access* **2024**, *12*, 19500–19509. [\[CrossRef\]](#)
- Akhtar, I.; Altamimi, A.; Khan, Z.A.; Alojaiman, B.; Alghassab, M.; Kirmani, S. Reliability Analysis and Economic Prospect of Wind Energy Sources Incorporated Microgrid System for Smart Buildings Environment. *IEEE Access* **2023**, *11*, 62013–62027. [\[CrossRef\]](#)
- Hu, J.; Shan, Y.; Yang, Y.; Parisio, A.; Li, Y.; Amjady, N.; Islam, S.; Cheng, K.W.; Guerrero, J.M.; Rodríguez, J. Economic model predictive control for microgrid optimization: A review. *IEEE Trans. Smart Grid* **2023**, *15*, 472–484. [\[CrossRef\]](#)
- Faraji, H.; Hemmati, R.; Siano, P. Resilience Control of DC Microgrid Integrated with Multi-Nanogrids Considering Connected-Islanded States. *CSEE J. Power Energy Syst.* **2024**, *10*, 786–796. [\[CrossRef\]](#)
- Mirzaeva, G.; Miller, D. DC and AC Microgrids for Standalone Applications. *IEEE Trans. Ind. Appl.* **2023**, *59*, 7908–7918. [\[CrossRef\]](#)
- Huang, T.; Wu, D.; Ilić, M. Cyber-Resilient Automatic Generation Control for Systems of AC Microgrids. *IEEE Trans. Smart Grid* **2024**, *15*, 886–898. [\[CrossRef\]](#)
- Gomez-Redondo, M.; Rivera, M.; Muñoz, J.; Wheeler, P. A Systematic Literature Review on AC Microgrids. *Designs* **2024**, *8*, 77. [\[CrossRef\]](#)
- Liu, Y.; Li, P.; Xing, Z.; Han, X.; Fu, Q.; Jiang, Z. Research on Microgrid Superconductivity-Battery Energy Storage Control Strategy Based on Adaptive Dynamic Programming. *IEEE Trans. Appl. Supercond.* **2024**, *34*, 1–4. [\[CrossRef\]](#)
- Saude, B.; LaSart, N.; Blair, J.; Beik, O. Microgrid-Based Wind and Solar Power Generation on Moon and Mars. *IEEE Trans. Smart Grid* **2023**, *14*, 1329–1332. [\[CrossRef\]](#)
- Sepasi, S.; Talichet, C.; Pramanik, A.S. Power Quality in Microgrids: A Critical Review of Fundamentals, Standards, and Case Studies. *IEEE Access* **2023**, *11*, 108493–108531. [\[CrossRef\]](#)
- Puchalapalli, S.; Singh, B.; Das, S. Synchronizing Control of Wind Turbine Driven Doubly Fed Induction Generator System with DG in Remote Area Involving Solar PV-Battery Energy Storage. *IEEE Trans. Ind. Appl.* **2023**, *59*, 5774–5783. [\[CrossRef\]](#)
- Levi, E. Multiphase Electric Machines for Variable-Speed Applications. *IEEE Trans. Ind. Electron.* **2008**, *55*, 1893–1909. [\[CrossRef\]](#)
- Yepes, A.G.; Lopez, O.; Gonzalez-Prieto, I.; Duran, M.J.; Doval-Gandoy, J. A comprehensive survey on fault tolerance in multiphase ac drives, Part 1: General overview considering multiple fault types. *Machines* **2022**, *10*, 208. [\[CrossRef\]](#)
- Yepes, A.G.; Gonzalez-Prieto, I.; Lopez, O.; Duran, M.J.; Doval-Gandoy, J. A comprehensive survey on fault tolerance in multiphase ac drives, Part 2: Phase and switch open-circuit faults. *Machines* **2022**, *10*, 221. [\[CrossRef\]](#)
- Yepes, A.G.; Fonseca, D.S.B.; Antunes, H.R.P.; López, O.; Marques Cardoso, A.J.; Doval-Gandoy, J. Discrimination Between Eccentricity and Interturn Faults Using Current or Voltage-Reference Signature Analysis in Symmetrical Six-Phase Induction Machines. *IEEE Trans. Power Electron.* **2023**, *38*, 2421–2434. [\[CrossRef\]](#)
- Vancini, L.; Mengoni, M.; Rizzoli, G.; Zarri, L.; Tani, A. Local Demagnetization Detection in Six-Phase Permanent Magnet Synchronous Machines. *IEEE Trans. Ind. Electron.* **2024**, *71*, 5508–5518. [\[CrossRef\]](#)
- Gonzalez, O.; Doval-Gandoy, J.; Ayala, M.; Maidana, P.; Medina, C.; Rodas, J.; Romero, C.; Delorme, L.; Maciel, R.; Gregor, R. Model Predictive Torque Control based on Virtual Vectors for Six-Phase Induction Machines. In Proceedings of the 2024 IEEE Transportation Electrification Conference and Expo (ITEC), Chicago, IL, USA, 19–21 June 2024; pp. 1–6. [\[CrossRef\]](#)
- Li, Y.; Gao, J.; Zhang, Z.; Wang, Q. Model-Based and Model-Free Predictive Active Damping for LCL-Type Active-Front-End Rectifiers. *IEEE Trans. Ind. Electron.* **2024**, *71*, 11754–11765. [\[CrossRef\]](#)
- Chakraborty, S.; Chakrabarti, A.; Maiti, D.; Biswas, S.K. Transformer Isolated Fault Tolerant Three Phase Active Front End Converter for EV Charging. *IEEE Trans. Transp. Electrification* **2024**, *10*, 2332–2341. [\[CrossRef\]](#)
- Wu, M.; Ding, L.; Xu, X.; Wang, K.; Lu, Q.; Li, Y.W. A Common-Mode Voltage Elimination Scheme by Reference Voltage Decomposition for Back-to-Back Two-Level Converters. *IEEE Trans. Ind. Electron.* **2024**, *71*, 4463–4473. [\[CrossRef\]](#)
- Lin, H.; Lin, C.; Xie, D.; Acuna, P.; Liu, W. A Counter-Based Open-Circuit Switch Fault Diagnostic Method for a Single-Phase Cascaded H-Bridge Multilevel Converter. *IEEE Trans. Power Electron.* **2024**, *39*, 814–825. [\[CrossRef\]](#)
- Solemanifard, S.; Chen, Y.X.; Lak, M.; Lee, T.L. A Novel Three-Step Commutation Method for Direct Matrix Converter Free from Inrush Current and Voltage Error. *IEEE Access* **2023**, *11*, 25020–25034. [\[CrossRef\]](#)
- Qazi, S.; Mir, T.N.; Bhat, A.H.; Singh, B. Predictive Algorithm for Control of Common Mode Voltage and Switching Frequency in Direct Matrix Converter Fed System. *IEEE Trans. Ind. Electron.* **2022**, *69*, 13316–13325. [\[CrossRef\]](#)
- Toledo, S.; Caballero, D.; Maqueda, E.; Cáceres, J.J.; Rivera, M.; Gregor, R.; Wheeler, P. Predictive Control Applied to Matrix Converters: A Systematic Literature Review. *Energies* **2022**, *15*, 7801. [\[CrossRef\]](#)
- Elmorshedy, M.F.; Xu, W.; El-Sousy, F.F.; Islam, M.R.; Ahmed, A.A. Recent achievements in model predictive control techniques for industrial motor: A comprehensive state-of-the-art. *IEEE Access* **2021**, *9*, 58170–58191.

26. Maqueda, E.; Toledo, S.; Caballero, D.; Gavilan, F.; Rodas, J.; Ayala, M.; Delorme, L.; Gregor, R.; Rivera, M. Speed control of a six-phase im fed by a multi-modular matrix converter using an inner ptc with reduced computational burden. *IEEE Access* **2021**, *9*, 160035–160047.
27. Toledo, S.; Maqueda, E.; Rivera, M.; Gregor, R.; Wheeler, P.; Romero, C. Improved predictive control in multi-modular matrix converter for six-phase generation systems. *Energies* **2020**, *13*, 2660. [[CrossRef](#)]
28. Dan, H.; Zeng, P.; Xiong, W.; Wen, M.; Su, M.; Rivera, M. Model predictive control-based direct torque control for matrix converter-fed induction motor with reduced torque ripple. *CES Trans. Electr. Mach. Syst.* **2021**, *5*, 90–99.
29. Zou, Y.; Zhang, L.; Xing, Y.; Zhang, Z.; Zhao, H.; Ge, H. Generalized Clarke Transformation and Enhanced Dual-Loop Control Scheme for Three-Phase PWM Converters Under the Unbalanced Utility Grid. *IEEE Trans. Power Electron.* **2022**, *37*, 8935–8947. [[CrossRef](#)]
30. Ebrahimi, A. A Contribution to the Theory of Rotating Electrical Machines. *IEEE Access* **2021**, *9*, 113032–113039. [[CrossRef](#)]
31. O'Rourke, C.J.; Qasim, M.M.; Overlin, M.R.; Kirtley, J.L. A Geometric Interpretation of Reference Frames and Transformations: dq0, Clarke, and Park. *IEEE Trans. Energy Convers.* **2019**, *34*, 2070–2083. [[CrossRef](#)]
32. Kummerow, A.; Alramlawi, M.; Dirbas, M.; Nicolai, S.; Bretschneider, P. Clark-Park Transformation based Autoencoder for 3-Phase Electrical Signals. In Proceedings of the 2023 IEEE PES Innovative Smart Grid Technologies Europe (ISGT EUROPE), Grenoble, France, 23–26 October 2023; pp. 1–5. [[CrossRef](#)]
33. Wei, Y.; Hossain, M.M.; Mantooth, A. Dynamic Characterizations of 650 V, 900 V and 1200 V SiC MOSFETs under Low Temperatures. In Proceedings of the 2022 IEEE Aerospace Conference (AERO), Big Sky, MT, USA, 5–12 March 2022; pp. 1–8. [[CrossRef](#)]
34. Texas Instruments. ISO5500: Isolated IGBT/MOSFET Gate Driver with 2.5—A Output. 2008. Available online: <https://www.ti.com/lit/ug/sllu136a/sllu136a.pdf> (accessed on 15 September 2024).
35. Minshen Wind Power. 5kW Horizontal Axis Pitch Control Systems Wind Turbine MSFD5000. Available online: <https://minshenwindturbine.en.made-in-china.com/product/VqcEpYZUXMrj/China-5kw-Horizontal-Axis-Pitch-Control-Systems-Wind-Turbine-MSFD5000-.html> (accessed on 15 September 2024).
36. Badoni, M.; Singh, A.; Pandey, S.; Singh, B. Fractional-Order Notch Filter for Grid-Connected Solar PV System with Power Quality Improvement. *IEEE Trans. Ind. Electron.* **2022**, *69*, 429–439. [[CrossRef](#)]
37. Raju, S.; Mohan, N. Switching Optimized Modulation for Direct Three-Level Matrix Converter. *IEEE Trans. Power Electron.* **2024**, *39*, 3313–3328. [[CrossRef](#)]
38. Wu, D.; Wang, P.; Lyu, Y.; Andersen, M.A.E.; Ouyang, Z. A High-Efficiency and High-Power-Density Partial Power Buck-Boost Converter. *IEEE J. Emerg. Sel. Top. Power Electron.* **2024**, *12*, 3563–3573. [[CrossRef](#)]
39. Carbone, L.; Marchesoni, M.; Passalacqua, M.; Vaccaro, L.; Formentini, A. H₂-LMI-Based High Performance Control for Matrix Converter. *IEEE Trans. Ind. Electron.* **2024**, *71*, 10029–10038. [[CrossRef](#)]

Disclaimer/Publisher's Note: The statements, opinions and data contained in all publications are solely those of the individual author(s) and contributor(s) and not of MDPI and/or the editor(s). MDPI and/or the editor(s) disclaim responsibility for any injury to people or property resulting from any ideas, methods, instructions or products referred to in the content.